Electrical and Computer Engineering Faculty Publications and Presentations

Department of Electrical and Computer Engineering

5-2024

Titanium Dioxide Nanomaterial Ink Production Through Laser Ablation Synthesis in Solution for Printed Electronics Applications

Devyn Duryea
Boise State University

Nicholas McKibben
Boise State University

Jacob Manzi
Boise State University

Taylor Brennan
Oregon State University

Harish Subbaraman
Boise State University

See next page for additional authors

Authors

Devyn Duryea, Nicholas McKibben, Jacob Manzi, Taylor Brennan, Harish Subbaraman, David Estrada, and Nirmala Kandadai

Titanium Dioxide Nanomaterial Ink Production Through Laser Ablation Synthesis in Solution for Printed Electronics Applications

Devyn Duryea,* Nicholas McKibben, Jacob Manzi, Taylor Brennan, Harish Subbaraman, David Estrada, and Nirmala Kandadai*

Flexible and printed electronics have become increasingly popular as they make possible the production of flexible, low-cost, multifunction devices that are unachievable through traditional manufacturing methods. The printed films are significantly impacted and thus limited by the existing ink production process. Herein, an alternate technique of generating high-quality titanium dioxide (TiO₂) nanoparticle ink compatible with aerosol jet printing using laser ablation synthesis in solution (LASiS) is showcased. Dynamic light scattering data and transmission electron microscopy confirm the particle size distribution. UV–vis measurements are performed, and the Beer–Lambert relationship is used to determine the concentration of the generated ink. The inks generated at two different repetition rates are compared: 200 kHz and 1 MHz. X-Ray diffraction analysis of the aerosol jet printed thin film post-thermal sintering confirms the grain size and phase purity of the printed thin films. This work demonstrates the effectiveness of the LASiS technique in producing printable nanoparticle inks with little-to-no postprocessing.

1. Introduction

Flexible and printed electronics (FPE) are fabricated by depositing functional materials on flexible substrates using additive manufacturing techniques to achieve novel performance features in applications such as wearable electronics,[1] structural health monitoring systems,[2] and even self-healing devices.[3] Biocompatible and biodegradable FPE devices have also been achieved using polymers that do not cause harm to the body and break down over time.[4] A common technique for FPE fabrication utilizes direct printing of nanoparticle (NP) inks. These NP inks used for fabrication are colloidal systems consisting of extremely fine particles, with diameters less than 200 nm, dispersed in a solvent vehicle. Although many materials can be formulated into NP inks and printed using a state-of-the-art materials printer for FPE applications, the quality of the printed materials is closely coupled to the ink synthesis process.

Some of the most widely used nanoparticle synthesis methods include citrate reduction,[5] block copolymer synthesis,[6] mechanical milling,[7] and spark ablation.[8] Although effective, these methods have significant drawbacks, such as using carrier gases or solvents,[9] using chemicals to create a reaction,[6] and managing mechanical properties that prevent some ductile materials from being milled.[10] These methods often include toxic chemicals and chemical precursors, consume large amounts of energy, and require high pressures and temperatures.[11] Synthesis methods for transition metals, in particular, most often include wet chemical synthesis,[5,12] reduction of organic precursors,[13] electrochemical synthesis,[14] and metal vapor synthesis.[15,16]

Laser ablation synthesis in solution (LASiS) is a method for creating NPs in a solvent.[17,18] LASiS is feasible due to the capability of a laser to localize a large amount of energy into a small volume.[19] At the laser's focal point, the high energy transforms

D. Duryea, J. Manzi, T. Brennan, H. Subbaraman, N. Kandadai
School of Electrical Engineering and Computer Science
Oregon State University
Corvallis, OR 97331, USA
E-mail: duryead@oregonstate.edu; nirmala.kandadai@oregonstate.edu

The ORCID identification number(s) for the author(s) of this article can be found under https://doi.org/10.1002/adem.202400721.

D. Duryea, J. Manzi, H. Subbaraman, N. Kandadai
Department of Electrical and Computer Engineering
Boise State University
Boise, ID 83712, USA

N. McKibben, D. Estrada
Micron School of Material Science and Engineering
Boise State University
Boise, ID 83725, USA

D. Estrada
Center for Advanced Energy Studies
Boise State University
Boise, ID 83725, USA

D. Estrada
Idaho National Laboratory
Idaho Falls, ID 83415, USA

the metal into a plasma state and ejects material from the rest of the bulk target. This area where the plasma is being created is often referenced in literature as a plasma plume.[20,21] The bulk sample is submerged in a solution, and as the plasma plume is being created, it is actively cooled by the solution surrounding it. This quenching changes the state of the plasma back into a solid nanomaterial dispersed in solution.[22] LASiS has the primary advantage of being environmentally friendly as it uses no harsh chemical reducers or precursors.[17,23,24] Furthermore, LASiS can be used to actively tune the desired particle loading of the NP ink[25] and embed dopant materials as it is being synthesized.[26] Aqueous NP inks created using only deionized (DI) water also eliminate the need for solvent exchange before printing. Low particle-loaded aqueous inks do not require binders or surfactants, allowing the production of smooth and high-purity printed thin films.[27] Therefore, low particle-loaded aqueous inks are often used to fabricate various optoelectronics such as transistors,[27,28] light-emitting diodes,[29] photodiodes,[29] and solar cells.[30,31]

NPs generated by LASiS are used in a multitude of applications, including catalysis[32] and biomedical applications.[33,34] Historically, the application of LASiS for generating ink for FPE has been limited due to the low NP volume production and lack of control over NP diameter.[35,36] In this work, we show that through careful manipulation of optomechanical properties in the LASiS system, we can generate a NP ink with a precise NP particle size distribution that can be directly used for FPE manufacturing.

While FPE can be fabricated using multiple different printing techniques, for our work, we selected aerosol jet printing (AJP) due to its versatility in printing a wide range of ink viscosities (1–1000 cP),[28,37,38] wide usage by the FPE community, and it provides good spatial resolution (≈10 μm).[36,37] During AJP, NP ink is aerosolized with an atomizer and printed using aerodynamic focusing.[37,39,40] AJP also offers other advantages, such as deposition onto nonplanar surfaces,[40] low material waste,[41,42] and compatibility with a wide range of materials.[37,43,44] Recently, AJP has been demonstrated for strain monitoring in soft structural materials,[45] fabrication of surface acoustic wave thermometers,[46] thermoelectric energy harvesters,[47] and wearable fold electrodes for biomonitoring.[48] In our work, we used an ultrasonic atomizer as it is compatible with extremely low-viscosity ink of 1–4 cP and provides high printing resolution.[37,49] The ultrasonic atomizer is also used for plasma jet printing[50–52] (PJP) and given the narrow distribution of nanoparticle diameters created by our technique, the ink rheology can quickly be adapted to become advantageous for use on other material jetting printers, such as inkjet printing and PJP.

NP production rate and concentration are critical to the final print's quality. In this work, we studied the production rate of LASiS ink, phase composition, and particle size distribution to demonstrate the successful production of titanium dioxide (TiO$_2$) NP ink using two different laser repetition rates: 200 kHz and 1 MHz. Experimental factors such as total ablation time and the velocity of the stage holding the sample were varied to analyze the effect on NP production rate. We further demonstrated successful AJP of NP inks while comparing postprocessing steps necessary to print a uniform thin film. We observed that while the NP ink produced utilizing a 200 kHz laser repetition rate is additive free and compatible with AJP without postprocessing, the NP size distribution is larger than the ink

generated with 1 MHz. Printing parameter optimization was implemented to achieve excellent print quality and particle uniformity. Printed films were thermally sintered and X-Ray diffraction (XRD) was used to determine the phase purity of the sintered thin film.

2. Results and Discussion

Utilizing a 7.5 cm focusing lens, a stage velocity of 2.6 mm s^{-1}, an average laser power of 3.0 W, and a bulk piece of titanium was submerged in 10 mL of DI water and irradiated with a 1040 nm Spirit-One femtosecond (fs) laser for 3 h to synthesize TiO$_2$ NPs. **Figure 1**a shows a bright-field image of the "as-synthesized" TiO$_2$ nanoparticles, obtained using a JOEL JEM-2100HR transmission electron microscope (TEM). High-resolution TEM imaging was performed to further characterize the particles (Figure 1b). Some inherent defects were observed within larger particles, and the interplanar spacing was measured to be 3.60 Å, which agrees with those reported in literature,[9,10] and is indicative of the (101) crystal plane of anatase-phase TiO$_2$. Additionally, NP diameter distribution analysis was performed (Figure 1c), resulting in an average diameter of 10.88 nm and a standard deviation of 10.39 nm.

The TiO$_2$ synthesis was performed again with a repetition rate of 200 kHz, with all other experimental parameters the same. Figure 1d shows a bright-field image of the "as-synthesized" TiO$_2$ nanoparticles, obtained using the TEM. High-resolution imaging was performed using a FEI Titan 80–200 TEM to observe the interplanar distance of NPs in the sample (Figure 1e). Defects were observed in the larger particles and an interplanar spacing was measured to be 3.26 Å. The NP diameter distribution for the 200 kHz repetition rate (Figure 1f) showed an average diameter of 39.63 and 20.99 nm.

Selected-area electron diffraction (SAED) was performed on a single TiO$_2$ NP created with a 1 MHz repetition rate (**Figure 2**a). Analysis of the polycrystalline diffraction pattern indicates that the NP is brookite phase TiO$_2$, as it matches within 2% error from the International Center for Diffraction Data (ICDD) world standard of 66.66% oxide and 33.33% titanium atomic percentage TiO$_2$. Additionally, SAED was performed on a TiO$_2$ NP created using a 200 kHz repetition rate (Figure 2b). The polycrystalline diffraction pattern indicates anatase phase TiO$_2$ as it matched within 5% error of the ICDD standard. The difference in the observed phase of the TiO$_2$ obtained from the electron diffraction calculations appears to indicate that multiple crystalline phases of TiO$_2$ were generated.

Dynamic light scattering (DLS) measurements were performed on the ink as DLS is a reliable method of finding NP hydrodynamic diameter while accounting for agglomeration and aggregates in the solution.[53,54] **Figure 3**a shows the NP size distribution for the 1 MHz repetition rate, with an average hydrodynamic diameter calculated to be 17.53 nm and a standard deviation of 21.46 nm agreeing within 7 nm of the average diameter calculated by TEM. The largest NP diameters were ≈155 nm. However, the predominant number of particle sizes followed a tight distribution from 12.25 to 13.55 nm. The low average NP size is promising for FPE applications as the characteristic
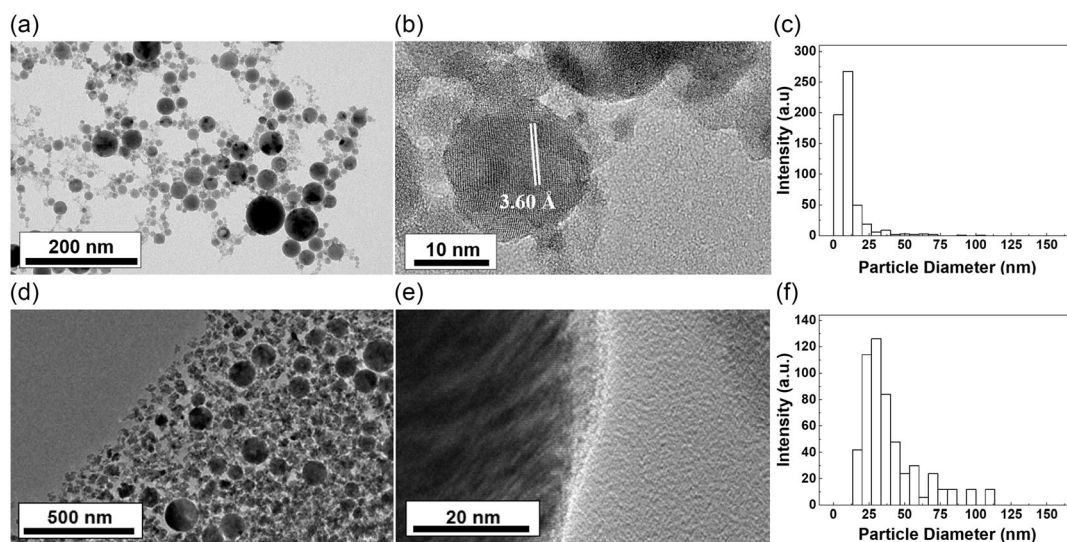
Figure 1. TiO$_2$ NP characterization created with a 1 MHz repetition rate with a) a bright-field image of the TiO$_2$, b) a high-resolution TEM image revealing some structural disorder within a single TiO$_2$ nanoparticle, a measured interplanar spacing of 3.60 Å, and c) a distribution of TEM NP diameter. TiO$_2$ NP characterization created with a 200 kHz repetition rate with d) a bright-field image of the TiO$_2$ NPs, e) a high-resolution TEM image revealing the interplanar spacing of 3.26 Å, and f) a distribution of TEM NP diameters.
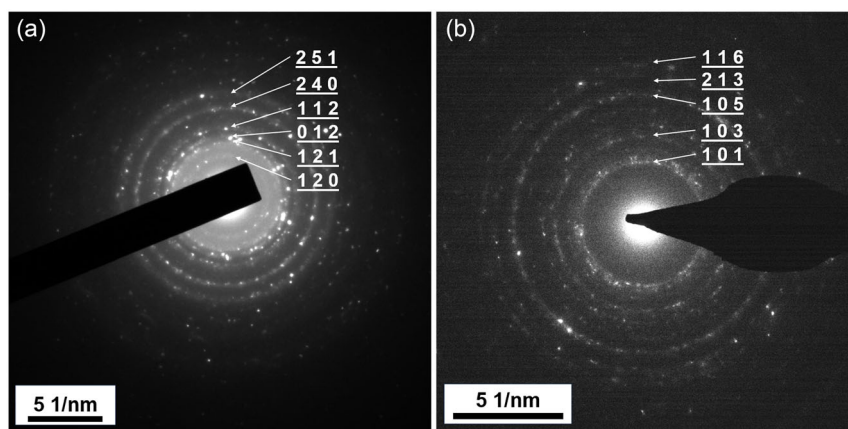
Figure 2. SEAD pattern of the TiO$_2$ NPs confirming phase composition of NPs created at repetition rates of a) 1 MHz and b) 200 kHz.
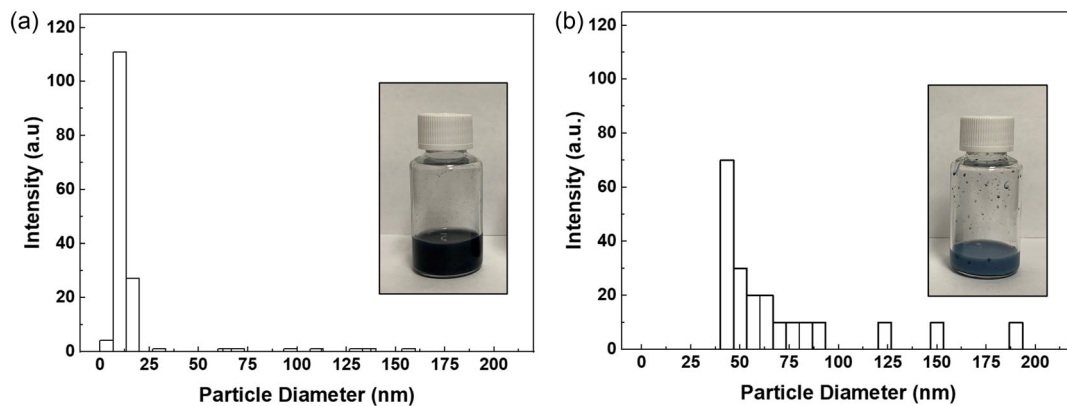
Figure 3. DLS distribution of hydrodynamic diameters of the TiO$_2$ NPs created by LASiS using a repetition rate of a) 1 MHz and b) 200 kHz. Insets show pictures of respective NP inks demonstrating a color difference.

**ADVANCED
SCIENCE NEWS**

www.advancedsciencenews.com

**ADVANCED
ENGINEERING
MATERIALS**

www.aem-journal.com

sintering time of the titanium NPs is less with smaller NP sizes.[55]

Figure 3b shows the NP size distribution generated by laser operation at a 200 kHz repetition rate, with an average hydrodynamic diameter calculated to be 62.10 nm and a standard deviation of 31.02 nm. The TiO_2 NPs generated at 200 kHz (inset of Figure 3b) appear blue in color, and the TiO_2 NPs generated at 1 MHz (inset of Figure 3a) appear darker blue or black. This correlates with early researchers[56] who have observed black TiO_2 NPs and have shown through UV–vis that the optical absorption properties of black TiO_2 NPs are enhanced for visible light absorption in comparison to the more traditional white TiO_2 NPs.

To determine the exact rate of nanoparticle production, we placed the NP ink solution inside a rotary evaporator (Rotavapor R-100). The sample was evaporated via a hot water bath until it was reduced to a dry nanopowder. This nano-powder was then weighed and reintroduced into DI water at controlled and known concentrations (**Figure 4**a). UV–vis measurements were performed using 388 nm light on different concentrations of TiO_2 ink to extract the extinction coefficient of 43.67 (ε^* cm^{-1}) proportional to the slope of the absorbance versus concentration curve. The Beer–Lambert Law was used as the governing equation for calculating the extinction coefficient of the TiO_2 NPs[57]

$$A = \varepsilon c l \tag{1}$$

where A is the absorbance, ε is the extinction coefficient of the material, c is the molar concentration of the material, and l is the path length.

The linear regression calculated from the Beer–Lambert relationship (Figure 4b) allowed concentration measurements for all future samples, based solely on UV–vis spectroscopy. One might notice the black color of the more concentrated TiO_2 samples in Figure 4a.

Test results of NP concentration based on the total time irradiated by the laser are shown in **Figure 5**a. The concentrations in mg mL^{-1} of the resulting TiO_2 ink after ablation over the time intervals ranging from 5 to 250 min are shown. Each of the 6 repetitions of the test in Figure 5 was performed with 10 mL of DI water and laser parameters of 1 MHz frequency, 3.0 W average power, and utilizing a 10 cm focal length plano-convex focusing lens. The speed of the motorized stage holding
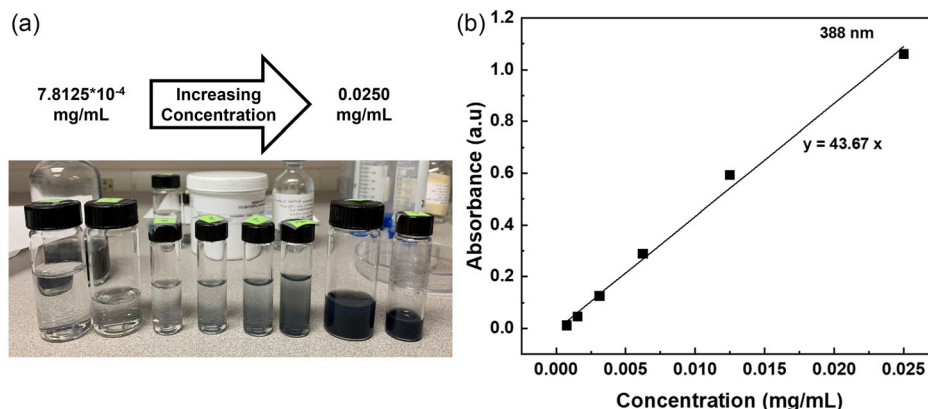
Figure 4. a) Photograph and table of TiO_2 dilutions in DI water at known concentrations. b) Beer–Lambert calibration curve of the TiO_2 NP ink with the extinction coefficient (43.67 cm^{-1}) proportional to the slope, as calculated by linear regression method from the absorbance versus concentration data.
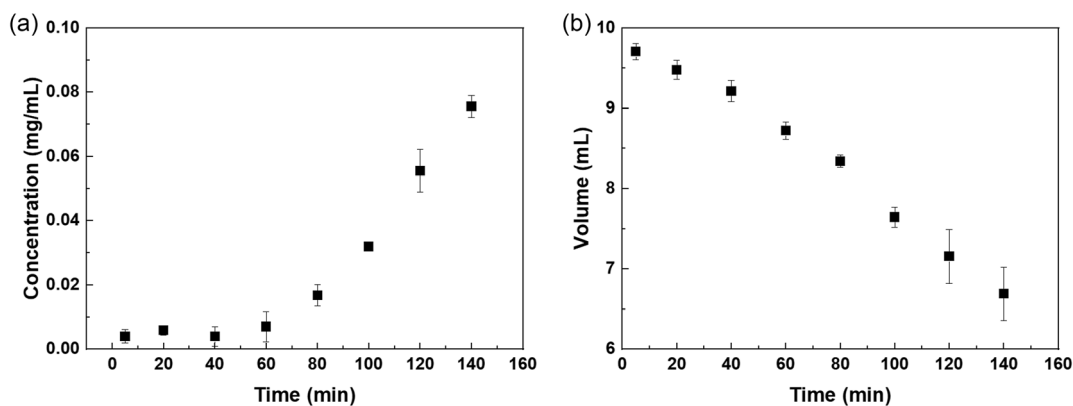
Figure 5. a) Plot of ink concentration versus time calculated by UV–vis spectroscopy. Data points are an average of three trials and error bars depict the standard deviation. b) Plot of evaporation over time directly from the LASiS process measured by UV–vis spectroscopy.

the sample was held constant at 2.5 mm s^{-1} for all iterations of the tests shown in Figure 5.

Two competing phenomena occur during nanoparticle production that directly affect the concentration. First, the accumulation of particles over time raises the concentration of NPs in the resulting solution. Second, the evaporation of the DI water in the solution causes an increase in the concentration measurements. As the laser hits the sample, it heats the surrounding solution and therefore evaporates the water out of the solution. A change in the focal length directly results from the evaporation of DI water as the laser light traverses a shorter overall distance to reach the target. To combat any significant change in the beam focus, and therefore the ablation rate, the evaporation rate of the LASiS process was measured (Figure 5b) over the same time intervals as Figure 5a. An evaporation rate of 0.02 mL min^{-1} or 1.2 mL h^{-1}. was observed. While producing a larger volume of ink for AJP, loss of focus due to evaporation was accounted for by adding ≈0.5 mL of DI water for every 30 min of laser ablation.

Next, we performed a test of the NP production rate by varying the velocity of the linear stage (**Figure 6**a,b). Here we ensured the volume of each sample was kept constant at 10 mL. The time interval per ablation was 40 min while the stage velocity varied from 0.5 mm s^{-1} up to 7.5 mm s^{-1}. The test was performed for 200 kHz repetition rate (Figure 6a) and 1 MHz (Figure 6b). All other factors including the average laser power were carefully kept consistent for each trial. The preliminary data shows an outlier for the 7.5 mm s^{-1} stage velocity (Figure 6a) resulting in a concentration of 0.318 mg. Overall, for the 200 kHz repetition rate, a positive relationship is observed between the velocity of the linear stage and the NP production rate with an average increase of 0.042 mg for every 1 mm s^{-1} increase in stage velocity. This is a ≈3× increase in production rate response to stage velocity compared to the 1 MHz repetition rate (Figure 6b).

The TiO$_2$ NP ink for this thin film was created with parameters of laser power at 3.0 W, 1 MHz frequency, and a stage velocity of 2.6 mm s^{-1}. The AJP was used to deposit TiO$_2$ in a serpentine pattern on a glass substrate using an Optomec Aerosol Jet 200 system. **Figure 7**a,b shows a 2 × 5 mm rectangular thin film comprising two-layer TiO$_2$ printed with a platen temperature of 50 °C and a gas focusing ratio (GFR = sheath gas flow/carrier gas flow) of 2.8. Visual inspection of the TiO$_2$ print in Figure 7b shows a high concentration of nanoparticles around the outside edge of the AJP printing path. The flow of particles inside the microdroplet determines the distribution of NPs as it dries. The forming of a ring of concentrated nanomaterial around the outside edge is commonly referred to as a
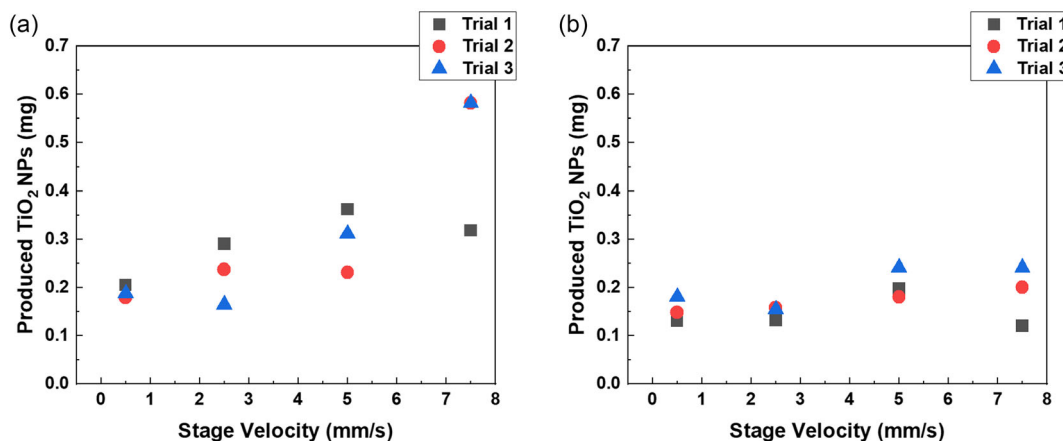
Figure 6. Linear stage velocity versus produced TiO$_2$ NPs (mg) in solution data found through UV–vis spectroscopy at a) 200 kHz repetition rate and b) 1 MHz repetition rate.
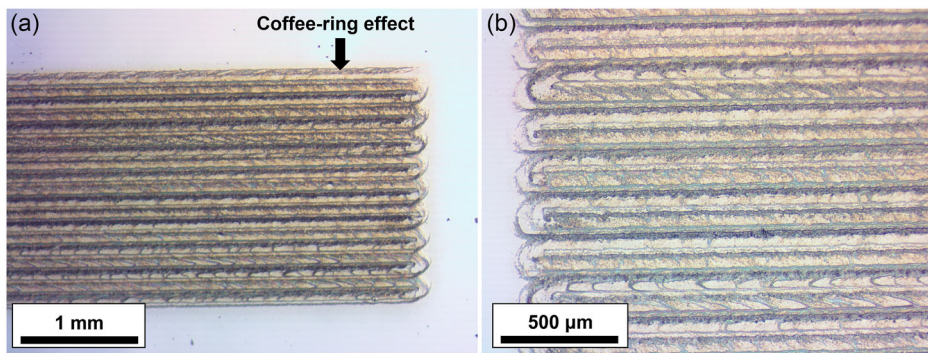
Figure 7. a) Microscope image of printed TiO$_2$ thin film. b) High-magnification image of the TiO$_2$ thin film. The AJP-printed films demonstrate a significant coffee ring effect.

**ADVANCED
SCIENCE NEWS**

www.advancedsciencenews.com

**ADVANCED
ENGINEERING
MATERIALS**

www.aem-journal.com

"coffee ring" effect and is the result of capillary flow.[58–60] The capillary flow induces internal currents in the droplet pushing the NPs toward the point where air, the droplet, and the substrate meet. Mixing water and diethylene glycol has been shown to induce a Marangoni flow in an inkjet-printed microdroplet which counteracts the capillary flow and produces a more uniform particle layer when thoroughly dried.[61] Our work proposes the induction of a Marangoni flow by mixing ethylene glycol (EG) and isopropyl alcohol (IPA) into the DI water–TiO_2 solution. NP dispersion testing was performed through drop casting 1 mL depositions of differing TiO_2 ink solutions onto a borosilicate glass slide. The different ink formulations were prepared by first ultrasonically agitating the pure TiO_2 and DI water solution for 20 min. The sonicated TiO_2 solution was then mixed with EG and IPA with concentrations measured by percent volume. The sample was immediately drop cast onto a hot plate surface heated to 50 °C. The platform was held at 50 °C for about 30 min until each ink mixture dried completely.

Figure 8a–d shows iterations of adding EG and IPA in differing concentrations. Figure 8a shows the dried TiO_2 ink after curing. A dark ring-like deposit of nanoparticles is evident around the droplet's outside edge, signifying a high concentration of particles. Figure 8b,c, with the addition of EG, show a high concentration of nanoparticles settling into the center of the droplet with the 4:1 TiO_2:EG volume ratio in Figure 8c, exhibiting the most even dispersion of nanomaterial throughout the droplet. Figure 8d, with the addition of EG and IPA, demonstrated a comparatively dramatic level of spreading. This is hypothesized to result from low surface tension in the droplet. From these results, we chose 4:1 TiO_2:EG to conduct further AJP printing trials.

Figure 9 shows the results of the 4:1 TiO_2:EG solution AJP with two layers. The thin film was printed into a 2 × 5 mm rectangle with a platen temperature of 50 °C, as well as a GFR of 3.9. Visual inspection of the 4:1 TiO_2:EG thin film printed on a glass slide in Figure 9 demonstrates less of a coffee ring effect in direct comparison to the TiO_2 absent of any alcohol. The measured AJP track width was about 71.42 μm. It is also evident that ink pooling occurs near the top edge of the thin film in the location where the print head of the AJP spent the most time.

Next, we printed the ink generated with parameters of laser power at 3.0 W, 200 kHz frequency, and a stage velocity of 2.6 mm s^{-1}, after laser ablation for 24 h using the same AJP. A 200 μm tip was used on the aerosol jet printer and the TiO_2 ink was printed under ambient conditions with an ink temperature of 25 °C. A GFR of 2 was selected to maximize the ink deposition rate,[62] while still achieving reasonable printed line resolution, and the platen was heated to 50 °C and higher to drive off excessive water before subsequent printer passes. Four printed passes were utilized to build up the TiO_2 structures with the total print time for the TiO_2 square being ≈2 h. Images of the printed TiO_2 square were captured using a Zeiss Axio Imager M2 with an Axiocam 305 digital camera. An EC Epiplan 10×/0.25 HD M27 objective was used to perform brightfield (**Figure 10**a), dark-field (Figure 10b), and circular differential interference contrast (C-DIC) (Figure 10c) imaging to visualize the printed film, shown in Figure 10a–c.

The TiO_2 NP ink produced free of any additives or postprocessing was aerosol jet printed as shown in **Figure 11**a. The coffee ring effect observed in the 1 MHz repetition rate sample was not observed in the 200 kHz print; therefore, no EG or any other precursors needed to be added before printing into a thin film.
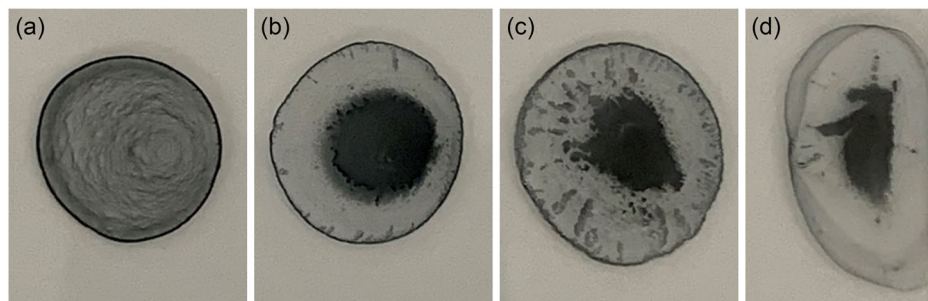
Figure 8. Drop-casted ink formulations: a) TiO_2 ink, b) 3:1 TiO_2:EG, c) 4:1 TiO_2:EG, and d) 4:1:1 TiO_2:EG:IPA by volume.
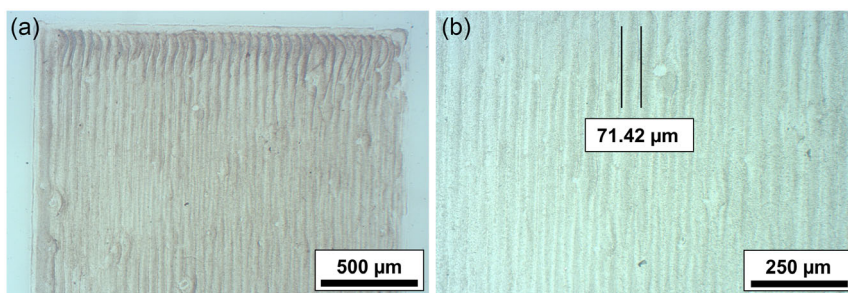
Figure 9. Microscope image of 4:1 TiO_2:EG ink AJP two layers thick demonstrating less coffee ring effect compared to the TiO_2 film absent of EG with a) 5× and b) 10× microscope objectives.
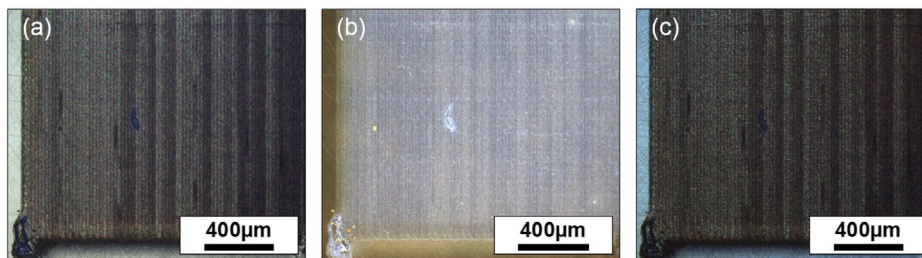
Figure 10. Microscope image of TiO$_2$ 1 × 1 cm square printed on sapphire for XRD analysis with a) bright-field, b) dark-field, and c) C-DIC imaging.
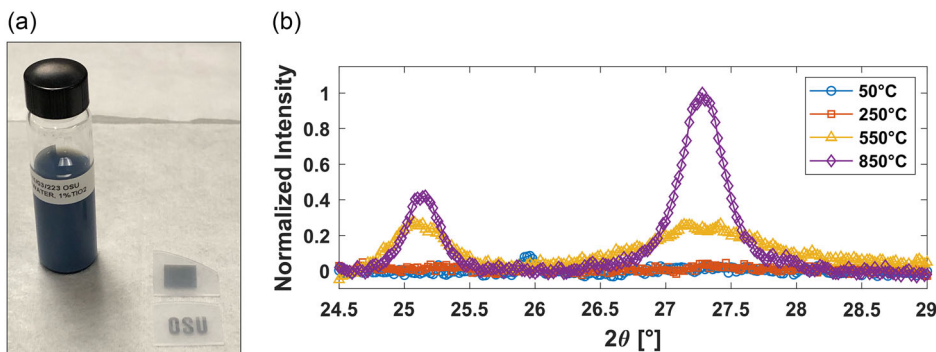
Figure 11. a) Picture of TiO$_2$ ink along with the square print and OSU print on sapphire. b) XRD analysis at sintering temperatures of 50, 250, 550, and 850 °C.

The TiO$_2$ deposition rate was low, due to the ink's low particle loading (10 mg mL^{-1}). However, the particle stability of the ink was observed to be good as no sedimentation was observed from the aqueous suspension throughout the printing session, highlighting good compatibility with the ultrasonic atomization of AJP and other printer modalities.[63,64] The particle stability due to the small size of the LASiS TiO$_2$ nanoparticles also indicates that higher loading TiO$_2$ inks may be stable as well for future ink formulations, thereby improving the material deposition rate. Despite the high particle stability, instrumental drift was still observed during the 4 h print session.[65] Therefore, the atomization current and print speed were dynamically adjusted to control the ink deposition rate, decreasing the atomization current and increasing print speed from 2 to 4 mm s^{-1} over time.

Sintering cycles were performed on the printed TiO$_2$ samples in a tube furnace under open air at temperatures of $T = 50$, 250, 550, and 850 °C, with a temperature ramp rate of 15 °C min^{-1} and a 30 min hold time at peak temperature for each iteration. A Rigaku Miniflex X-Ray diffractometer was used to perform measurements on the printed TiO$_2$ square before sintering and in between heating cycles to assess the grain size and phase of the thin film. A copper source was used to generate X-rays (1.541 Å), and the sample was measured in the scan range of $2\theta = 24°–48°$ with a step size of 0.02°. XRD spectra were aligned using the sapphire peak at 41.6°, and the plots (Figure 11b) were cropped to accentuate the 101 and 110 R peaks of TiO$_2$ related to the anatase (observed in TEM) and rutile phases respectively.[66] These characteristic peaks were not visible in the spectra for the sintering conditions of 50 and 250 °C, denoting that the material

is amorphous and not crystalline for these sintering temperatures. Notably, a small degree of anatase character was observed in the spectra at 38.2° prior to thermal treatment, which became more visible after treatment at 250 °C. However, quantifying exact values was difficult due to the noise and proximity of the sapphire peak; therefore, the results were treated qualitatively to support TEM observations. Once the sample was heated to 550 °C, broad peaks emerged, which sharpened at 850 °C, exhibiting the rutile and anatase phase of TiO$_2$.

Scherrer equation was utilized to estimate the grain size of the printed thin film, postprocessed at 550 and 850 °C.[67]

$$\tau = \frac{k\lambda}{\beta \cos \theta} \tag{2}$$

where τ is the calculated grain size, k is a dimensionless shape factor set to 0.89 for spherical particles, λ is the wavelength of the X-rays generated from the source, β represents the full width at half maximum of the XRD peak, and θ is the Bragg angle. Based on the 101 peaks, $\tau_{(101),550\,°C} = 17.77$ nm and $\tau_{(101),850\,°C} = 29.20$ nm. Based on the rutile peak, $\tau_{(110R),550\,°C} = 9.09$ nm and $\tau_{(110R),850\,°C} = 21.75$ nm.

Figure 12a quantifies the total crystallinity of the TiO$_2$ thin film exposed to various thermal sintering temperatures and normalized against the final crystallinity when sintered at 850 °C. Figure 12b shows the biphasic results for the thin film sintered at 550 and 850 °C, further distinguishing the degree of crystallinity by phase. The XRD crystallinity and phase results are summarized in Figure 12c, confirming ≈75% rutile to ≈25% anatase phase in the final crystalline TiO$_2$ film.

**ADVANCED
SCIENCE NEWS**

www.advancedsciencenews.com

**ADVANCED
ENGINEERING
MATERIALS**

www.aem-journal.com

Thermal Treatment [°C]	Normalized Crystallinity	Anatase	Rutile
50	0	0	0
250	0	0	0
550	0.7051	0.2421	0.463
850	1	0.2498	0.7502
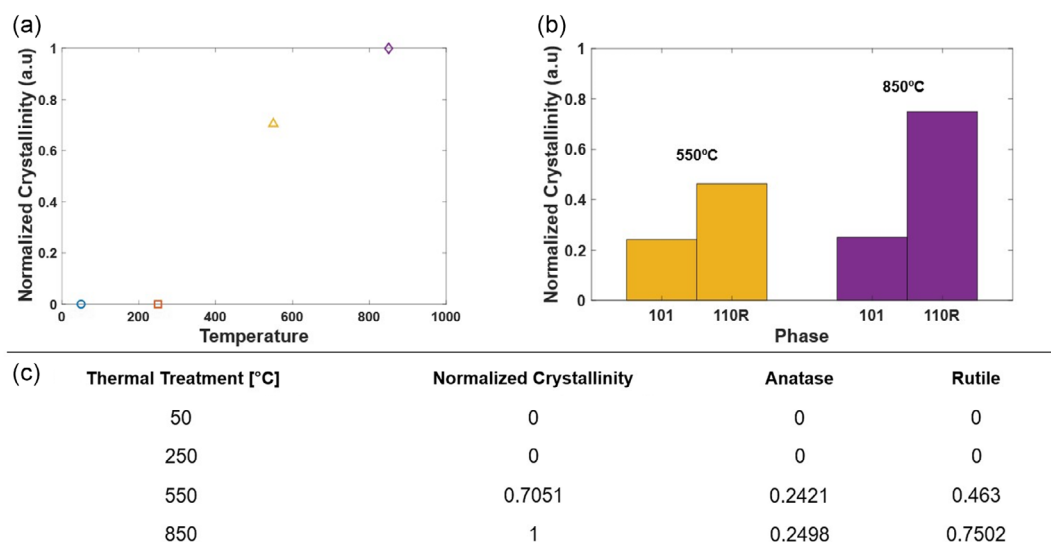
Figure 12. a) Scatter plot of the TiO$_2$ film's total crystallinity normalized to the sample sintered at 850 °C. b) Bar chart depicting the biphasic results for the TiO$_2$ thin film sintered at 550 and 850 °C. c) Table summarizing the crystallinity and phase data.
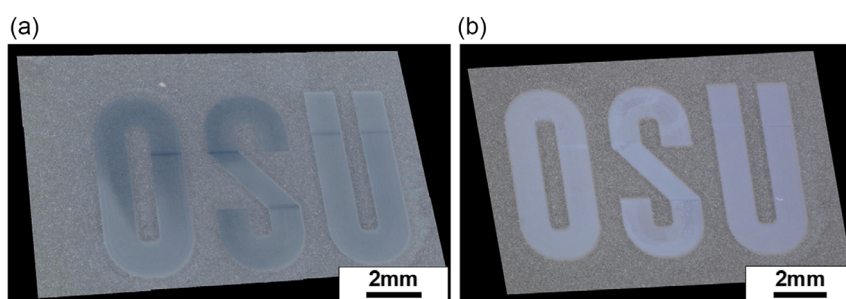
Figure 13. a) Microscope image of OSU on sapphire prior to sintering. b) Microscope image of OSU on sapphire postsintering at 850 °C for 30 min.

Additionally, a Keyence VHX 7000 microscope was used to image the Oregon State University (OSU) print prior to sintering (**Figure 13**a) and postsintering in (Figure 13b) to investigate coverage and highlight the flexibility of design for AJP and the TiO$_2$ nanoparticle ink. Along with the enhanced uniformity due to sintering at 850 °C, a color change from light blue resembling the TiO$_2$ ink to a white color signifying a crystalline thin film of TiO$_2$ was observed.

3. Conclusion

In conclusion, we have reported a process of creating TiO$_2$ NP inks directly through LASiS with a fs laser. Through optimization of the ink production process, TiO$_2$ NP ink was successfully produced for 1 MHz and 200 kHz laser repetition rates, with a narrow NP diameter distribution and a viscosity compatible with an aerosol jet printer. The results indicate that the LASiS method described in this work can be used in the synthesis of NP inks with a high degree of consistency in ink properties. UV–vis concentration data displayed an increased NP production rate as a result of a decrease in repetition rate from 1 MHz to 200 kHz

while average laser power remained at 3.0 W. For NP ink produced at 1 MHz, the addition of ethylene glycol directly into the solution was shown to be effective in improving printability and minimizing the coffee-ring effect. The NP ink produced at a 200 kHz laser repetition rate eliminated the need for precursors before printing into a uniform thin film. XRD revealed a primarily rutile phase TiO$_2$ and fully crystalline TiO$_2$ thin films after sintering at 850 °C. Our research has shown that the LASiS process provides a feasible route toward the creation of versatile, high-quality nanoparticle-based inks for use with flexible electronics applications.

4. Experimental Section

The experimental setup to generate TiO$_2$ nanoparticle ink is shown in **Figure 14**. A 2 mm-diameter beam from a Spirit-One, 400 fs, 1040 nm laser at two different repetition rates of 200 kHz and 1 MHz was focused by a 7.5 cm focal length lens onto a bulk titanium sample (1.3 g) mounted onto a linear stage. A half-waveplate and polarizer combination was used to control the laser power precisely. The bulk sample was held in a borosilicate glass Petri dish filled with 10 mL of DI water. The laser beam was tightly focused onto the surface of the titanium sample. DI water was chosen as the liquid media to ensure the resulting solution's purity.
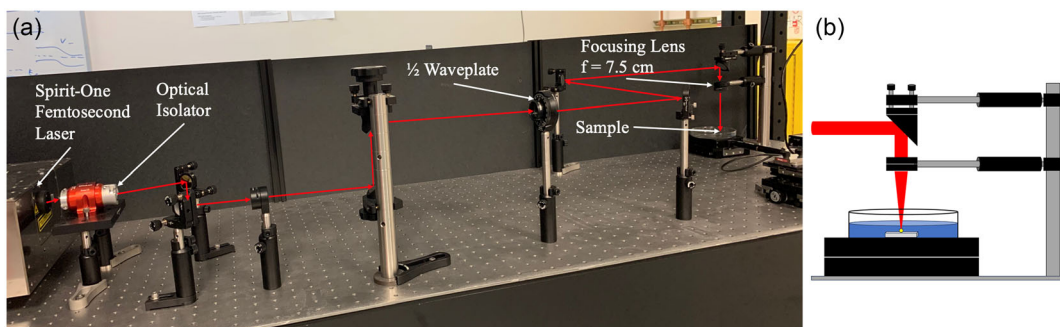
Figure 14. Laboratory setup for LASiS with a fs laser to produce nanomaterial ink. a) Image of fs pulses from a Spirit-One laser (red line) routed to the sample by a series of mirrors and a half waveplate for power modulation. b) Diagram of laser path through the focusing lens onto the sample submerged in DI water.

The velocity of the linear stage supporting the sample was controlled by a Thorlabs actuator (Z825B) to move the area of contact between the laser light and bulk titanium target during NP production. After ablation, the bulk sample was removed, and the remaining colloidal TiO_2 NP solution was used for characterization and printing on an Optomec Aerosol Jet 200.

Conflict of Interest

The authors declare no conflict of interest.

Data Availability Statement

The data that support the findings of this study are available from the corresponding author upon reasonable request.

[1] B. Nie, S. Liu, Q. Qu, Y. Zhang, M. Zhao, J. Liu, *Acta Biomater.* **2022**, *139*, 280.

[2] X. Liu, Y. Wei, Y. Qiu, *Micromachines* **2021**, *12*, 695.

[3] H. Huang, L. Han, X. Fu, Y. Wang, Z. Yang, L. Pan, M. Xu, *Small* **2021**, *17*, 2006807.

[4] H. Liu, R. Jian, H. Chen, X. Tian, C. Sun, J. Zhu, Z. Yang, J. Sun, C. Wang, *Nanomaterials* **2019**, *9*, 950.

[5] J. Turkevich, P. C. Stevenson, J. Hillier, *Discuss. Faraday Soc.* **1951**, *11*, 55.

[6] T. Sakai, P. Alexandridis, *Langmuir* **2004**, *20*, 8426.

[7] L. C. Damonte, L. A. Mendoza Zélis, B. Marí Soucase, M. A. Hernández Fenollosa, *Powder Technol.* **2004**, *148*, 15.

[8] T. V. Pfeiffer, J. Feng, A. Schmidt-Ott, *Adv. Powder Technol.* **2014**, *25*, 56.

[9] J. F. Sánchez-Ramírez, U. Pal, L. Nolasco-Hernández, J. Mendoza-Álvarez, J. A. Pescador-Rojas, *J. Nanomater.* **2008**, *2008*, 1.

[10] B. Alinejad, Y. Zare, in *Abrasive Technology – Characteristics And Applications* (Ed: A. Rudawska), InTech, London, UK **2018**.

[11] R. Vishwanath, B. Negi, *Curr. Res. Green Sustainable Chem.* **2021**, *4*, 100205.

[12] M. Daka, M. Ferrara, M. Bevilacqua, P. Pengo, P. Rajak, R. Ciancio, T. Montini, L. Pasquato, P. Fornasiero, *ACS Appl. Nano Mater.* **2022**, *5*, 4710.

[13] F. T. Ladipo, G. K. Anderson, *Organometallics* **1994**, *13*, 303.

[14] M. T. Reetz, W. Helbig, *J. Am. Chem. Soc.* **1994**, *116*, 7401.

[15] P. L. Timms, *J. Chem. Educ.* **1972**, *49*, 782.

[16] J. You, M. D. Hossain, Z. Luo, *Nano Convergence* **2018**, *5*, 26.

[17] V. Amendola, M. Meneghetti, *Phys. Chem. Chem. Phys.* **2009**, *11*, 3805.

[18] G. W. Yang, *Prog. Mater. Sci.* **2007**, *52*, 648.

[19] A. Balachandran, S. P. Sreenilayam, K. Madanan, S. Thomas, D. Brabazon, *Results Eng.* **2022**, *16*, 100646.

[20] S. Chander, S. K. Tripathi, *Mater. Adv.* **2022**, *3*, 7198.

[21] S. Dai, Y. Wu, T. Sakai, Z. Du, H. Sakai, M. Abe, *Nanoscale Res. Lett.* **2010**, *5*, 1829.

[22] F. Taccogna, *J. Plasma Phys.* **2015**, *81*, 495810509.

[23] D. Amans, M. Diouf, J. Lam, G. Ledoux, C. Dujardin, *J. Colloid Interface Sci.* **2017**, *489*, 114.

[24] D. Zhang, B. Gökce, S. Barcikowski, *Chem. Rev.* **2017**, *117*, 3990.

[25] D. Z. Duryea, N. Kandadai, in *2023 IEEE Inter. Flexible Electronics Technology Conf. (IFETC)*, IEEE, San Jose **2023**, pp. 01–03.

[26] D. Duryea, N. Kandadai, *AIP Adv.* **2022**, *12*, 095011.

[27] V. Subramanian, J. Cen, A. de la Fuente Vornbrock, G. Grau, H. Kang, R. Kitsomboonloha, D. Soltman, H.-Y. Tseng, *Proc. IEEE* **2015**, *103*, 567.

**ADVANCED
SCIENCE NEWS**

www.advancedsciencenews.com

**ADVANCED
ENGINEERING
MATERIALS**

www.aem-journal.com

[28] B. Mishra, Y. M. Chen, *Nanomaterials* **2022**, *12*, 4487.

[29] J. Jan, J. Zhu, J. Ting, A. C. Arias, *Adv. Funct. Mater.* **2022**, *32*, 2112343.

[30] J. Krzemiński, J. Dominiczak, D. Baraniecki, D. Janczak, T. Raczyński, J. Ostapko, M. Jakubowska, *Crystals* **2021**, *11*, 1184.

[31] S. K. Karunakaran, G. M. Arumugam, W. Yang, S. Ge, S. N. Khan, X. Lin, G. Yang, *J. Mater. Chem. A* **2019**, *7*, 13873.

[32] F. Waag, Y. Li, A. R. Ziefuß, E. Bertin, M. Kamp, V. Duppel, G. Marzun, L. Kienle, S. Barcikowski, B. Gökce, *RSC Adv.* **2019**, *9*, 18547.

[33] G. Lentini, E. Fazio, F. Calabrese, L. M. De Plano, M. Puliafico, D. Franco, M. S. Nicolò, S. Carnazza, S. Trusso, A. Allegra, F. Neri, C. Musolino, S. P. P. Guglielmino, *Biosens. Bioelectron.* **2015**, *74*, 398.

[34] G. Drummen, R. Zamiri, A. Zakaria, H. Ahangar, M. Darroudi, G. Zamiri, Z. Rizwan, *Int. J. Nanomed.* **2013**, 233.

[35] V. Amendola, M. Meneghetti, *Phys. Chem. Chem. Phys.* **2013**, *15*, 3027.

[36] T. E. Itina, *J. Phys. Chem. C* **2011**, *115*, 5044.

[37] A. A. Gupta, A. Bolduc, S. G. Cloutier, R. Izquierdo, in *2016 IEEE Inter. Symp. on Circuits and Systems (ISCAS)*, IEEE, Montréal, QC **2016**, p. 866.

[38] M. Smith, Y. S. Choi, C. Boughey, S. Kar-Narayan, *Flex. Print. Electron.* **2017**, *2*, 015004.

[39] T. Seifert, E. Sowade, F. Roscher, M. Wiemer, T. Gessner, R. R. Baumann, *Ind. Eng. Chem. Res.* **2015**, *54*, 769.

[40] M. Davies, M. J. Hobbs, J. Nohl, B. Davies, C. Rodenburg, J. R. Willmott, *Sci. Rep.* **2022**, *12*, 18496.

[41] B. King, M. Renn, in Aerosol Jet® Direct Write Printing for Mil-Aero Electronic Applications, **2008**.

[42] M. Serpelloni, E. Cantù, M. Borghetti, E. Sardini, *Sensors* **2020**, *20*, 841.

[43] I. Grunwald, E. Groth, I. Wirth, J. Schumacher, M. Maiwald, V. Zoellmer, M. Busse, *Biofabrication* **2010**, *2*, 014106.

[44] C. E. Folgar, C. Suchicital, S. Priya, *Mater. Lett.* **2011**, *65*, 1302.

[45] K. T. Fujimoto, J. K. Watkins, T. Phero, D. Litteken, K. Tsai, T. Bingham, K. L. Ranganatha, B. C. Johnson, Z. Deng, B. Jaques, D. Estrada, *NPJ Flex. Electron.* **2020**, *4*, 1.

[46] N. McKibben, B. Ryel, J. Manzi, F. Muramutsa, J. Daw, H. Subbaraman, D. Estrada, Z. Deng, *Microsyst. Nanoeng.* **2023**, *9*, 1.

[47] C. Hollar, Z. Lin, M. Kongara, T. Varghese, C. Karthik, J. Schimpf, J. Eixenberger, P. H. Davis, Y. Wu, X. Duan, Y. Zhang, D. Estrada, *Adv. Mater. Technol.* **2020**, *5*, 2000600.

[48] T. Valayil Varghese, J. Eixenberger, M. Rajabi-Kouchi, M. Lazouskaya, C. Francis, H. Burgoyne, K. Wada, H. Subbaraman, D. Estrada, *ACS Mater. Au* **2024**, *4*, 65.

[49] S. P. Sreenilayam, É. McCarthy, L. McKeon, O. Ronan, R. McCann, K. Fleischer, B. Freeland, V. Nicolosi, D. Brabazon, *Chem. Eng. J.* **2022**, *449*, 137817.

[50] J. Manzi, N. Kandadai, R. P. Gandhiraman, H. Subbaraman, *IEEE Trans. Electron. Devices* **2023**, *70*, 1548.

[51] J. Manzi, T. Varghese, A. Dhamala, L. Prakasan, J. Eixenberger, N. Kandadai, D. Estrada, H. Subbaraman, in *2023 IEEE Inter. Flexible Electronics Technology Conf. (IFETC)*, IEEE, Piscataway, NJ **2023**, pp. 1–3.

[52] J. Manzi, A. E. Weltner, T. Varghese, N. McKibben, M. Busuladzic-Begic, D. Estrada, H. Subbaraman, *Nanoscale* **2023**, *15*, 6596.

[53] T. G. F. Souza, V. S. T. Ciminelli, N. D. S. Mohallem, *J. Phys.: Conf. Ser.* **2016**, *733*, 012039.

[54] B. K. Wilson, R. K. Prud'homme, *J. Colloid Interface Sci.* **2021**, *604*, 208.

[55] B. Buesser, A. J. Gröhn, S. E. Pratsinis, *J. Phys. Chem. C* **2011**, *115*, 11030.

[56] V. A. Zuñiga-Ibarra, S. Shaji, B. Krishnan, J. Johny, S. Sharma Kanakkillam, D. A. Avellaneda, J. A. A. Martinez, T. K. D. Roy, N. A. Ramos-Delgado, *Appl. Surf. Sci.* **2019**, *483*, 156.

[57] D. F. Swinehart, *J. Chem. Educ.* **1962**, *39*, 333.

[58] R. D. Deegan, O. Bakajin, T. F. Dupont, G. Huber, S. R. Nagel, T. A. Witten, *Nature* **1997**, *389*, 827.

[59] R. D. Deegan, O. Bakajin, T. F. Dupont, G. Huber, S. R. Nagel, T. A. Witten, *Phys. Rev. E* **2000**, *62*, 756.

[60] M. Majumder, C. S. Rendall, J. A. Eukel, J. Y. L. Wang, N. Behabtu, C. L. Pint, T.-Y. Liu, A. W. Orbaek, F. Mirri, J. Nam, A. R. Barron, R. H. Hauge, H. K. Schmidt, M. Pasquali, *J. Phys. Chem. B* **2012**, *116*, 6536.

[61] J. Park, J. Moon, *Langmuir* **2006**, *22*, 3506.

[62] A. Mahajan, C. D. Frisbie, L. F. Francis, *ACS Appl. Mater. Interfaces* **2013**, *5*, 4856.

[63] N. J. Wilkinson, M. A. A. Smith, R. W. Kay, R. A. Harris, *Int. J. Adv. Manuf. Technol.* **2019**, *105*, 4599.

[64] Y. Huang, L. Jiang, B. Li, P. Premaratne, S. Jiang, H. Qin, *J. Manuf. Process.* **2020**, *56*, 1270.

[65] D. Yoo, C. M. Mahoney, J. R. Deneault, C. Grabowski, D. Austin, J. D. Berrigan, N. Glavin, P. R. Buskohl, *Prog. Addit. Manuf.* **2021**, *6*, 257.

[66] D. A. H. Hanaor, C. C. Sorrell, *J. Mater. Sci.* **2011**, *46*, 855.

[67] A. L. Patterson, *Phys. Rev.* **1939**, *56*, 978.